Emergence of spatially periodic diffusive waves in small-world neuronal networks

Qinglong L. Gu

School of Mathematical Sciences, MOE-LSC, and Institute of Natural Sciences, Shanghai Jiao Tong University, Shanghai, China

Yanyang Xiao

Courant Institute of Mathematical Sciences, New York University, New York, New York 10012, USA
and NYUAD Institute, New York University Abu Dhabi, Abu Dhabi, United Arab Emirates

Songting Li[*]

School of Mathematical Sciences, MOE-LSC, and Institute of Natural Sciences, Shanghai Jiao Tong University, Shanghai, China

Douglas Zhou[†]

School of Mathematical Sciences, MOE-LSC, and Institute of Natural Sciences, Shanghai Jiao Tong University, Shanghai, China

It has been observed in experiment that the anatomical structure of neuronal networks in the brain possesses the feature of small-world networks. Yet how the small-world structure affects network dynamics remains to be fully clarified. Here we study the dynamics of a class of small-world networks consisting of pulse-coupled integrate-and-fire (I&F) neurons. Under stochastic Poisson drive, we find that the activity of the entire network resembles diffusive waves. To understand its underlying mechanism, we analyze the simplified regular-lattice network consisting of firing-rate-based neurons as an approximation to the original I&F small-world network. We demonstrate both analytically and numerically that, with strongly coupled connections, in the absence of noise, the activity of the firing-rate-based regular-lattice network spatially forms a static *grating pattern* that corresponds to the spatial distribution of the firing rate observed in the I&F small-world neuronal network. We further show that the spatial grating pattern with different phases comprise the continuous attractor of both the I&F small-world and firing-rate-based regular-lattice network dynamics. In the presence of input noise, the activity of both networks is perturbed along the continuous attractor, which gives rise to the diffusive waves. Our numerical simulations and theoretical analysis may potentially provide insights into the understanding of the generation of wave patterns observed in cortical networks.

I. INTRODUCTION

Neuronal networks exhibit rich dynamics. For example, waves of neuronal activity have been observed in multiple brain areas and brain states across species [1–3], which can be either spontaneously generated or evoked by external stimuli [4,5]. In addition, neuronal population activity can synchronize and oscillate [6,7] to support rich cognitive functions [8]. And the membrane potential of individual neurons in the network has been observed to switch between up and down states under certain brain conditions [9–11]. The alternating activity is believed to be crucial for sensory signal processing [12–14], which may correlate with the bistability of neuronal dynamics [15] and the spike-timing-dependent adaption process [16]. At present, the mechanisms underlying many of these dynamical phenomena are under active investigation.

It is believed that the rich dynamics of neuronal networks are intimately related to the corresponding network structures, i.e., cortical connections linking individual neurons and neuronal populations are a key determinant of the capacity of the cortex to generate complex network dynamics. Accordingly, many studies have theoretically investigated the influence of network structure with specific types of connections on the dynamics of neuronal networks. For instance, it has been found that slow and fast oscillations can emerge in a sparsely and randomly connected network [17]. In other studies, by accounting for the fact that neurons prefer connecting locally to their neighbors, various localized connectivity kernels have been used to investigate network dynamics. Traveling waves can be generated when the connectivity kernel possesses an exponential decay structure [18,19]. Localized bump activity has been observed when the connectivity kernel follows a Gaussian profile [20]. In addition, static periodic structure can be generated when the connectivity kernel takes the shape of a Mexican hat [21].

In addition to the aforementioned properties of cortical connections, neuronal networks have been observed to possess the prominent property of small-world networks [22,23] with high clustering coefficients and short path lengths [24] in various brain areas across species. For instance, the small-world property has been identified in the full connectivity matrix of nematode *Caenorhabditis elegans* [25], macaque

[*]songting@sjtu.edu.cn
[†]zdz@sjtu.edu.cn

visual cortex [26], cat thalamocortical circuit [27], and the human brain [28]. As the small-world topology minimizes wiring costs in the brain meanwhile keeping high dynamical complexity [29], it is of great interest to investigate network dynamics with small-world connectivity in the experimental and computational neuroscience fields.

The influence of small-world structure on neuronal network dynamics has been investigated previously. It has been shown that small-world structure can induce or influence particular dynamics, e.g., synchronization dynamics and self-sustained dynamics in the integrate-and-fire neuronal network [30,31]. Moreover, the small-world topology can affect the spike mode of neurons in the excitatory Hodgkin-Huxley neuronal network [32], and the network clustering properties have strong relevance to the decision-making accuracy in a firing rate neuronal network [33]. In addition to neuronal networks, there are studies showing that the dynamics of epidemic and rumor spreading among agents can also be highly influenced by small-world network properties [34,35]. In particular, small-world networks are found to present a much faster disease propagation than regular-lattice networks [36].

In this work, we numerically and analytically investigate how the small-world structure generated from the effective rewiring of regular-lattice networks gives rise to the dynamics of spontaneous waves in the network. The article is organized as follows. In Sec. II, we introduce the integrate-and-fire (I&F) network model, the generation of network connectivity, and the simulation algorithm of network dynamics. In Sec. III, we numerically investigate the dynamics of small-world networks composed of I&F neurons, and find that the activity of the entire network resembles diffusive waves, and the activity of an individual neuron alternates between up and down states when the coupling strength is sufficiently strong. In Sec. IV, we analyze the simplified firing-rate-based regular-lattice network model to extract the mechanism underlying the observed dynamical phenomena in our simulations of the I&F small-world networks, and further show that the spatial *grating pattern* with different phases comprise the continuous attractor of the dynamics in both the I&F small-world networks and firing-rate-based regular-lattice networks. In Sec. V, we explore the dynamics of small-world networks by varying the network sparsity and dimension. Finally, in Sec. VI, we discuss the implications of our work and its novelty in contrast to previous works.

II. NETWORK MODELS AND SIMULATION ALGORITHMS

A. Integrate-and-fire neuronal model

The I&F neuronal network model has been applied to capture many dynamical phenomena observed in large-scale neuronal assemblies [17,37–40]. The neuronal network in our simulations is composed of both excitatory (E) and inhibitory (I) neurons. The governing equation for the membrane potential v_i^k of the ith neuron in the kth population ($k = E, I$) is

$$\frac{dv_i^k}{dt} = -g_L(v_i^k - \epsilon_R) + I_i^k(t), \qquad (1)$$

where ϵ_R is the resting voltage, g_L is the leak conductance, and $I_i^k(t)$ is the input current. The voltage v_i^k evolves according to Eq. (1) when $v_i^k < \epsilon_T$, where ϵ_T is the firing threshold. As v_i^k crosses ϵ_T, the neuron sends a pulse input to its connected downstream neurons at the time when v_i^k reaches ϵ_T; meanwhile v_i^k is reset to its resting voltage ϵ_R. Upon resetting, v_i^k immediately follows Eq. (1) again. In our simulations, we choose $g_L = 50 \text{ s}^{-1}$. In addition, the dimensionless values of the voltages are set as $\epsilon_R = 0.0$, $\epsilon_T = 1.0$ [41,42].

The input current injected into the ith neuron of the kth population consists of three parts,

$$I_i^k(t) = I_i^{k\text{Ext}}(t) + I_i^{kE}(t) + I_i^{kI}(t), \qquad (2)$$

where $I_i^{k\text{Ext}}(t) = f^k \sum_s \delta(t - \zeta_{is}^k)$ is the feed-forward external input, $I_i^{kE}(t) = J^E \sum_{j=1}^{N^E} C_{ij}^{kE} \sum_s \delta(t - \tau_{js}^E)$ is the recurrent excitatory input from neurons in the network, and $I_i^{kI}(t) = -J^I \sum_{j=1}^{N^I} C_{ij}^{kI} \sum_s \delta(t - \tau_{js}^I)$ is the recurrent inhibitory input from neurons in the network. Here $\delta(\cdot)$ is the Dirac delta function, f^k is the strength of the external input to a neuron in the kth population, and J^l is the coupling strength between a neuron and its upstream neurons from the lth population ($k, l = E, I$). The coupling constant $C_{ij}^{kl} = 1$ or 0 is an element in the connectivity matrix of the network that describes whether there exists a connection from the upstream jth neuron in the lth population to the downstream ith neuron in the kth population. The spike-time sequence $\{\zeta_{is}^k\}$ from the external input to the ith neuron in the kth population is generated by a stochastic Poisson process with rate ν^k. The feed-forward external Poisson input to each neuron in the network is generated independently. The spike-time sequence $\{\tau_{js}^k\}$ of the recurrent input is the time of the sth spike from the jth neuron in the kth population ($k = E, I$) generated from the network dynamics.

B. Network connectivity

We consider a network of N^E excitatory neurons and N^I inhibitory neurons. For the construction of a one-dimensional small-world network, we first uniformly place all the excitatory neurons in a line (0,1] with the ith excitatory neuron located at $x = i/N^E$, and we take the same procedure for all the inhibitory neurons. Then, we apply a distance-dependent algorithm [43] to generate network connectivity including the regular-lattice and small-world types. The details of the algorithm are described below. We first calculate the distance between the ith neuron in the kth population and the jth neuron in the lth population defined as $d_{ij}^{kl} = 2 \min(|i/N^k - j/N^l|, 1 - |i/N^k - j/N^l|)$. We then calculate the probability that an edge from the jth neuron in the lth population to the ith neuron in the kth population exists as

$$p(C_{ij}^{kl} = 1) = \beta p_0^l + (1 - \beta)\Theta(p_0^l - d_{ij}^{kl}), \qquad (3)$$

where $\Theta(\cdot)$ is the Heaviside function, and p_0^l is the parameter representing the sparsity of the network. For example, $p_0^l = 0$ corresponds to a network with no connections, and $p_0^l = 1$ corresponds to a network with all-to-all connections. Note that, we set p_0^l to be only dependent on the upstream neuron type l ($l = E, I$). The parameter β is the rewiring probability representing the chance of long-range connections. For
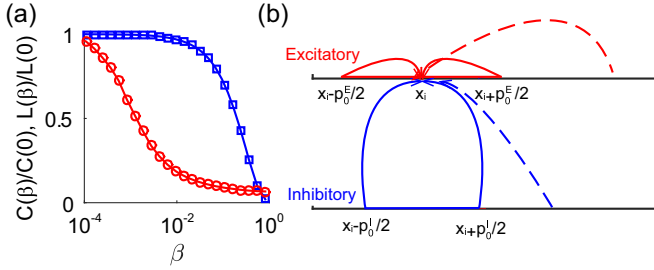
FIG. 1. The network connectivity. (a) Average path length $L(\beta)$ (red circles) and clustering coefficient $C(\beta)$ (blue squares) in the networks generated by Eq. (3) (normalized by their values in the regular-lattice limit) as function of β. We choose $N^E = N^I = 10^4$ and $p_0^E = p_0^I = 0.1$. (b) The small-world connectivity profile. The neuron located at x_i ($= i/N$) prefers to receive links from its local neighbors, i.e., presynaptic excitatory neurons located in the range $[x_i - p_0^E/2, x_i + p_0^E/2]$ (red) and presynaptic inhibitory neurons located in the range $[x_i - p_0^I/2, x_i + p_0^I/2]$ (blue). In addition, due to the small-world property, there also exist a few long-range connections (dashed lines).

example, as shown in Fig. 1(a), $\beta = 0$ corresponds to a regular-lattice network where neurons are locally connected with one another only when the distance among them is short. It can be seen that the regular-lattice network possesses a high clustering coefficient and a long average path length among neurons; $\beta = 1$ corresponds to an Erdös-Rényi random network where each neuron is globally connected with other neurons with equal probability despite the distance among them. It can be seen that the Erdös-Rényi random network possesses a low clustering coefficient and a short average path length among neurons; and a small β value (e.g., $0.001 < \beta < 0.1$) corresponds to a small-world network with both high clustering coefficients and short path lengths. In our simulations, we set $\beta = 0.01$ to generate small-world networks. The connectivity profile of the small-world networks is shown in Fig. 1(b).

Finally, we generate the connections between any two neurons based on the connection probability calculated by Eq. (3). We repeat the process for all pairs of neurons to generate networks with the structures of regular-lattice and small-world properties for our simulations. It has been shown [43] that this process is equivalent to the rewiring process in a regular-lattice network proposed in Ref. [25]. We thus refer to this process as the *effective rewiring process*.

C. Simulation algorithms

The simulation of the I&F neuronal network is carried out by the event-driven algorithm [44] that achieves machine accuracy. The event-driven algorithm for Poisson process as external inputs proceeds by generating the time of the next external spike. When a neuron receives an external spike, its voltage will increase. If the voltage exceeds the threshold, this neuron is said to fire at the time when its voltage reaches the threshold and sends pulse input to its downstream neurons. Its voltage is then held at the reset level, and the voltages of its downstream neurons are instantaneously increased (for excitatory inputs) or decreased (for inhibitory inputs). It is

possible that the voltages of these downstream neurons may now cross the threshold as well. In such a case, these neurons also fire. Subsequently, their voltages are held at the reset level, meanwhile their downstream neurons' voltages are changed. This process repeats until no new neurons fire. We emphasize that in our dynamics we hold the voltage of the neurons that just fired at the reset level in order to prevent any of these neurons from firing more than once at any given time. After all the neurons are updated at the current simulation time, we release these neurons from the reset voltage to follow the dynamics governed by Eq. (1) until the next external spike.

III. SIMULATIONS OF I&F NEURONS IN SMALL-WORLD NETWORKS

Here we perform the simulation of pulse-coupled I&F neurons in a network with small-world structure. When the recurrent input strength is small, as shown in Fig. 2(a), neurons fire irregularly and asynchronously. This activity pattern has been commonly observed in many theoretical studies [45,46] and experimental recordings [47]. As the input strength increases, after crossing a critical value, the network starts to spatially form multiple active clusters in the line (0, 1). Neurons within each cluster fire actively, and neurons between each cluster stay silent. As shown in Fig. 2(b), these active clusters are approximately evenly spaced during a time period of hundreds of milliseconds. We refer to this network activity as the grating pattern. We note that this grating pattern has also been observed in other networks with different connectivity structures [19,48]. However, the mechanisms underlying this pattern generation have not been fully studied. For instance, the grating pattern is found to be related to the instability of the system with positive eigenvalues [19,48]. Yet how the spatial frequency of the grating pattern is determined remains unclear. Interestingly, when the network evolves for hundreds of seconds, the active clusters start to move up and down continuously, as shown in Fig. 2(c). And these active clusters remain approximately evenly spaced during their movement. Consequently, if we randomly select a neuron and record its membrane potential trace, we can observe clear transitions between active and inactive states, i.e., up and down states, as shown in Fig. 2(d).

We next quantitatively characterize the properties of the grating pattern observed in the simulations of I&F small-world neuronal network dynamics. Within a short time period, the grating pattern is found to be nearly static. In addition, as shown in Fig. 2(e), it can be approximated by a periodic function $r(x) = r_{\max}[1 + \cos(\omega x + \phi)]/2$, where ω and ϕ capture the spatial frequency and the phase of the grating pattern, respectively. To characterize the long-time behavior of the grating pattern, we divide a long time period into several short time periods, and calculate the frequency and phase values in each short time period correspondingly. In particular, the phase is calculated sequentially along time and, in each time period, it is chosen to be the value closest to the phase value in the previous time period. Therefore, the phase value can go beyond the range of $[0, 2\pi]$. It has been found in our simulations that the frequency is time invariant but the phase is time dependent. Therefore, we can use the phase value to parametrize the dynamics of the grating pattern.
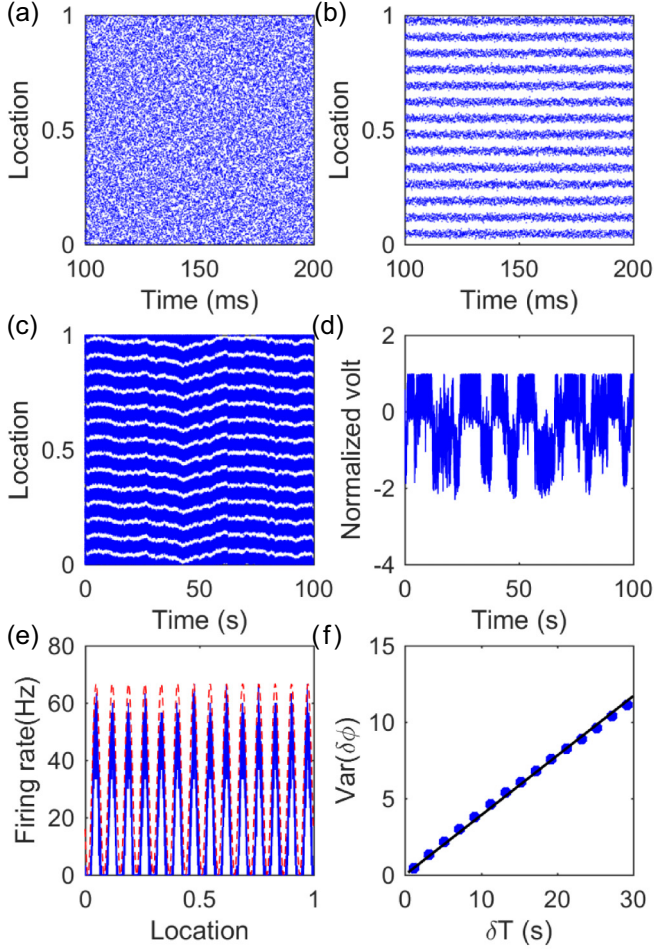
FIG. 2. Dynamics of I&F neurons in a small-world network. (a)–(c) Spike rasters of all the excitatory neurons. (a) is the case of weak connection and (b) and (c) are the cases of strong connection. (b) and (c) show the short- and long-time behavior of the network, respectively. (d) Normalized membrane potential of a sample neuron that exhibits transitions between up and down states as time evolves. (e) The spatial profile of the network firing activity in the line (0,1) (blue) fitted by the function $r(x) = r_{\max}[1 + \cos(\omega x + \phi)]/2$ (red). The time-averaged firing rate of each neuron is obtained from (b). (f) Variance of phase difference $\delta\phi$ as a function of time increment δT. The blue dots are obtained from the simulation in the I&F small-world neuronal network, and the black line is the linear fitting with slope 0.39. We set $J^E = 0.001$, $\nu^E = \nu^I = 3$ kHz for (a) and $J^E = 0.01$, $\nu^E = \nu^I = 6.7$ kHz for (b)–(f). Other parameters are $p_0^E = p_0^I = 0.1$, $N^E = N^I = 10^4$, $f^E = f^I = 0.03$, and $J^I = 2J^E$. Here the dynamics of the inhibitory population is almost the same as that of the excitatory population shown above.

We then calculate the difference between two phases corresponding to the start and the end of each long time period with length δT. As shown in Fig. 2(f), the variance of the phase change is nearly proportional to the time increment δT, i.e.,

$$\mathrm{Var}(\delta\phi) = 2D\delta T,$$

where D is a constant. This linear relation indicates that the phase dynamics of the network firing activity is a diffusion

process. We next perform a theoretical analysis to investigate the mechanism underlying the generation of the grating pattern and the diffusive activity of the I&F small-world neuronal network.

IV. ANALYSIS OF THE MECHANISM UNDERLYING NETWORK DYNAMICS

A. The emergence of the grating pattern

For the ease of analysis, we introduce the firing-rate-based neuronal model as an approximation to the I&F neuronal model. The firing rate dynamics of the ith neuron in the kth population is the following:

$$\tau_r \frac{dr_i^k}{dt} = -r_i^k + \Phi(\mu_i^k(t)), \tag{4}$$

where $\mu_i^k(t)$ is the total current input to the ith neuron in the kth population, and $\Phi(\cdot)$ is the transfer function that describes the relationship between an input and the corresponding neuronal firing rate response. The transfer function has the threshold-linear function form $\Phi(x) = (x - x_0)\Theta(x - x_0)$ which has similar features to the gain curve of the I&F neuron. Here $\Theta(\cdot)$ is the Heaviside function. This kind of nonlinear transfer function has been studied previously [49–51]. In addition, x_0 is the effective threshold and τ_r is the time constant of the firing rate. In this work, we take $x_0 = g_L/2$ and $\tau_r = 2$ ms.

As shown in Fig. 3(a), we find that the approximation is quite good for the single neuron dynamics. In addition, according to Eq. (2), the total input is given by

$$\mu_i^k(t) = f^k \nu^k + J^E \sum_{j=1}^{N^E} C_{ij}^{kE} r_j^E(t)$$

$$- J^I \sum_{j=1}^{N^I} C_{ij}^{kI} r_j^I(t) + \sigma^k \xi_i^k(t),$$

where f^k, J^E, J^I, and C_{ij}^{kl} are defined in the same way as those in the I&F neuronal model, ν^k is a constant corresponding to the rate of the Poisson input to the I&F neurons in the kth population, and r_j^l is the time-dependent firing rate of the jth neuron in the lth population. The fluctuations of the external input into the ith neuron in the kth population are modeled as Gaussian white noise denoted by $\sigma^k \xi_i^k(t)$, where $(\sigma^k)^2$ is the variance and $\langle \xi_i^k(s)\xi_j^l(t)\rangle = \delta_{kl}\delta_{ij}\delta(s - t)$. As shown in Figs. 3(b) and 3(c), when choosing the same parametric values as those in Fig. 2(b), we can also obtain the grating pattern in the firing-rate-based neuronal network [Eq. (4)]. In the following analysis, we first consider the case without the external input noise, i.e., $\sigma^k = 0$.

We write the firing rate of all the neurons as a vector $\mathbf{r}$ of size $(N^E + N^I)$ whose first N^E elements are the firing rate of excitatory neurons and the remaining N^I elements are that of inhibitory neurons. Correspondingly, we rewrite C_{ij}^{kl} (for $1 \leqslant i \leqslant N^k$, $1 \leqslant j \leqslant N^l$, and $k, l = E, I$) by C_{ij} (for $1 \leqslant i, j \leqslant N^E + N^I$). The connectivity of all the neurons can then be rewritten as a matrix $\mathbf{W}$ of size $(N^E + N^I) \times (N^E + N^I)$
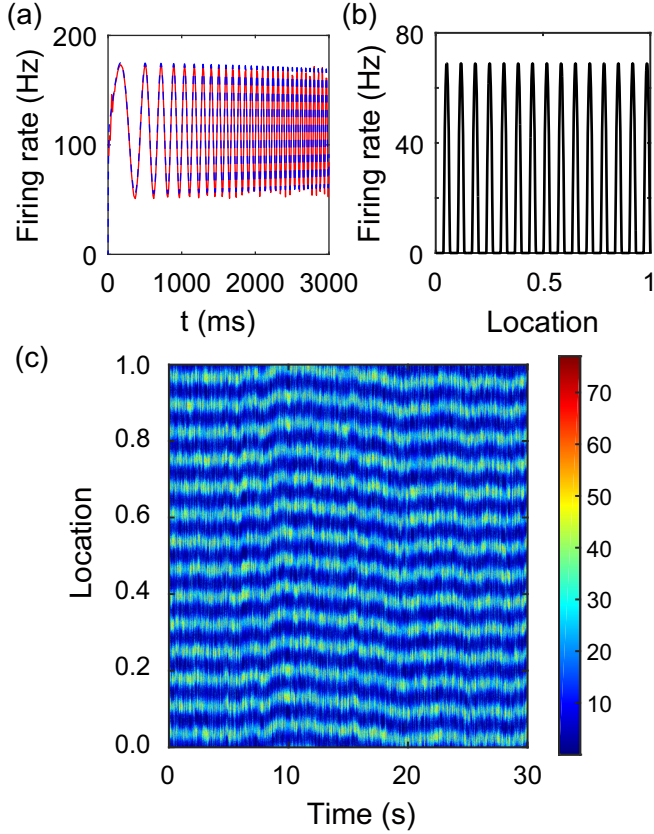
FIG. 3. Dynamics of the firing-rate-based neuron model. (a) Comparison of firing rates between the single firing-rate-based neuron and the I&F neuron. While receiving the inhomogeneous Poisson train with rate $14 + 6 \sin[0.002\pi(1 + 9t/3000)t]$ kHz, the mean firing rates of the firing-rate-based neuron and the I&F neuron are calculated over 10^4 trials. The red line is for the I&F neuron, and the blue dashed line is for the firing-rate-based neuron. The strength of the Poisson input is fixed as 0.01. (b) The spatial profile of the excitatory neurons' activity for a firing-rate-based small-world network in the line $(0, 1]$ in Eq. (4) for a given time without noise. The parametric values in (b) are chosen the same as those in Fig. 2(b). (c) Spatiotemporal profile of the excitatory neurons' activity in the same system as (b) while considering the noise of the external input. According to the Poisson external input into the I&F neuron, the variance of the external input into the firing-rate-based neuron takes the value of $(\sigma^k)^2 = (f^k)^2 \nu^k$, where f^k and ν^k are the strength and rate of a Poisson input in the kth population, respectively.

with the element in the ith row and jth column $W_{ij} = J_{ij}C_{ij}$. Here, $J_{ij} = J^E$ for $j \leqslant N^E$, while $J_{ij} = -J^I$ for $j > N^E$.

We note that, when the input strength is small, each neuron in the small-world I&F network exhibits irregular firing activity as shown in Fig. 2(a). The ability to fire indicates that each neuron receives a positive input. In such a case, the transfer function Φ in Eq. (4) is linear. Consequently, Eq. (4) can be rewritten as

$$\tau_r \frac{d\mathbf{r}}{dt} = (\mathbf{W} - \mathbf{I})\mathbf{r} + \mathbf{b}, \qquad (5)$$
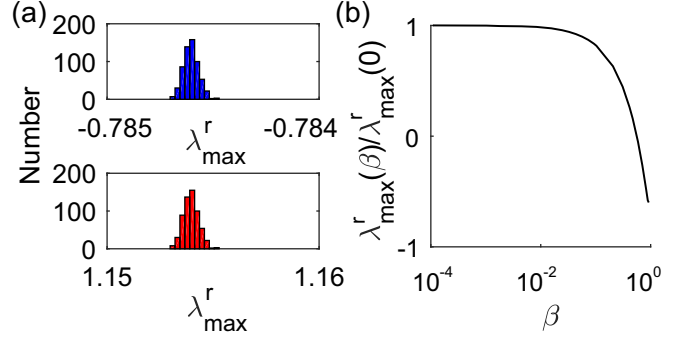

FIG. 4. The real part of the largest eigenvalue in different connectivity matrices. (a) The real part of the largest eigenvalue $\lambda_{\max}^r$ of networks with the rewiring probability $\beta = 0.01$ over 600 trials for $J^E = 0.001$ (upper) and $J^E = 0.01$ (lower). The parameters in the upper panel are chosen to be the same values as those in Fig. 2(a). The parameters in the lower panel are chosen to be the same values as those in Fig. 2(b). (b) The ratio of mean $\lambda_{\max}^r$ of $(\mathbf{W} - \mathbf{I})$ with nonzero rewiring probability β over trials to that of a regular-lattice network. The parameters here are set to be the same as those in Fig. 2(b). For each value of β, the mean largest eigenvalue is calculated over 600 trials.

where $\mathbf{b}$ is a vector of size $(N^E + N^I)$ whose first N^E elements equal $(f^E \nu^E - g_L/2)$, and the remaining N^I elements equal $(f^I \nu^I - g_L/2)$. Here $\mathbf{I}$ is the identity matrix of size $(N^E + N^I) \times (N^E + N^I)$. We define the maximum eigenvalue and its real part of $(\mathbf{W} - \mathbf{I})$ as $\lambda_{\max}$ and $\lambda_{\max}^r$, respectively. Note that the sign of $\lambda_{\max}^r$ determines the stability of Eq. (5). Only when $\lambda_{\max}^r$ is negative can the irregular firing activity exist and be stable in the I&F neuronal network. Consistently, the eigenvalue corresponding to the irregular pattern in Fig. 2(a) takes a negative real part $\lambda_{\max}^r \approx -0.7846 \pm (4 \times 10^{-5})$ as shown in the upper panel of Fig. 4(a). When $\lambda_{\max}^r$ is positive, Eq. (5) is no longer stable. In this case, we expect the emergence of the grating pattern because otherwise the I&F network remains stable and so is Eq. (5) based on the aforementioned argument. Consistently, the eigenvalue corresponding to the grating pattern in Fig. 2(b) takes a positive real part $\lambda_{\max}^r \approx 1.154 \pm (4 \times 10^{-4})$ as shown in the lower panel of Fig. 4(a). Meanwhile, as shown in Figs. 3(b) and 3(c), we indeed can find the spatially periodic solution to Eq. (4) (grating pattern) in such a case. Therefore, the sign of $\lambda_{\max}^r$ indicates the stability of dynamical patterns generated both in the firing-rate-based and the I&F small-world neuronal network.

As shown in Fig. 1(b), the small-world network in our simulations is generated by adding a few long-range connections to a locally connected network whose structure is close to regular lattice. Therefore, it can be expected that the eigenvalues of $(\mathbf{W} - \mathbf{I})$ corresponding to the two networks are close to each other. As shown in Fig. 4(b), the ratio of the real part of the largest eigenvalue of a network with nonzero rewiring probability β to that of a regular-lattice network with zero rewiring probability approaches unity as β tends to zero. The small-world network has a small but nonzero β ($\beta = 0.01$ in our simulations), thus the real part of its

largest eigenvalue can be well approximated by that of the regular-lattice network.

Based on the above results, the dynamical property of the small-world network shall be similar to that of the regular-lattice network. Therefore, we next turn to the analysis of the grating pattern in the regular-lattice network.

B. Spatial frequency of the grating pattern

To analyze the spatial profile of the grating pattern in the regular-lattice network, we further simplify the system of Eq. (4) by considering the asymptotic limit of large network size. When the network size is sufficiently large, the input current $\mu_i^k(t)$ can be expressed in terms of convolution as

$$\mu^k(x,t) = f^k(x)v^k + J^E N^E w^{kE}(x) * r^E(x,t)$$
$$- J^I N^I w^{kI}(x) * r^I(x,t)$$

for $x = i/N^k \in (0,1]$, where $w^{kE}(x)$ and $w^{kI}(x)$ are rectangular kernels satisfying the periodic boundary conditions,

$$w^{kl}(x) = \Theta\left(p_0^l/2 - \min(|x|, 1-|x|)\right), \quad (6)$$

and $*$ denotes spatial convolution. Thus Eq. (4) has the following continuous form:

$$\tau_r \frac{dr^k(x,t)}{dt} = -r^k(x,t) + \Phi(\mu^k(x,t)). \quad (7)$$

By assuming that the total input to all neurons is large, we simplify Eq. (7) as

$$\tau_r \frac{dr^k(x,t)}{dt} = -r^k(x,t) + \mu^k(x,t) - \frac{1}{2}g_L. \quad (8)$$

We next analyze Eq. (8) in the Fourier domain [taking the Fourier transform of x, $\tilde{f}(n) = \int_\Omega e^{-2\pi x n i} f(x)dx$]. For each Fourier mode n, we can obtain the coefficient matrix

$$A(n) = \begin{bmatrix} -1 + J^E N^E p_0^E \frac{\sin(\pi n p_0^E)}{\pi n p_0^E} & -J^I N^I p_0^I \frac{\sin(\pi n p_0^I)}{\pi n p_0^I} \\ J^E N^E p_0^E \frac{\sin(\pi n p_0^E)}{\pi n p_0^E} & -1 - J^I N^I p_0^I \frac{\sin(\pi n p_0^I)}{\pi n p_0^I} \end{bmatrix},$$

in which the first and second rows are obtained from the Fourier transforms of Eq. (8) when $k = E, I$, respectively. The matrix has two eigenvalues $\lambda_1(n) = -1$ and

$$\lambda_2(n) = -1 + J^E N^E p_0^E \frac{\sin(\pi n p_0^E)}{\pi n p_0^E} - J^I N^I p_0^I \frac{\sin(\pi n p_0^I)}{\pi n p_0^I}.$$

Substituting the relations of the parameters used in our simulations $p_0^E = p_0^I = p_0$, $N^E = N^I = N$, and $J^E = J^I/2 = J$ into the expression of $\lambda_2(n)$, we can further simplify $\lambda_2(n)$ as

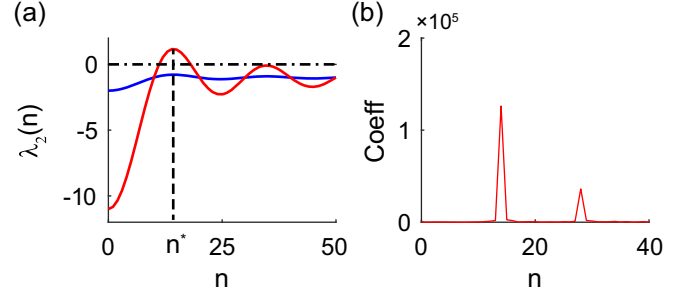$$\lambda_2(n) = -1 - JNp_0 \frac{\sin(\pi n p_0)}{\pi n p_0}. \quad (9)$$

FIG. 5. The influence of the eigenvalue λ_2 on the spatial frequency of the grating pattern. (a) $\lambda_2(n)$ for small and large connection strengths. $J^E = 0.001$ for the blue curve and $J^E = 0.01$ for the red curve. Other parameters are chosen to be the same as that in Fig. 2. The black dash-dotted line is the reference line $y = 0$. The eigenvalue $\lambda_2 \approx 1.1624$ at $n^* = 14$. (b) The Fourier coefficients of the I&F small-world network activity in Fig. 2(e). The global peak corresponds to the spatial frequency of the grating pattern $n^* = 14$, which is consistent with n^* obtained from (a).

From the above expression, $\lambda_2(n)$ can be greater than zero for certain n when the recurrent input strength J is large, which has been confirmed in Fig. 5(a). The condition of large input strength is supported by experimental observations [52].

In the case of large coupling strength, the solution to Eq. (8) will diverge because of the positiveness of the eigenvalue $\lambda_2(n)$ for certain n. Therefore, the linear dynamics of Eq. (8) may greatly deviate from that of the nonlinear I&F network. However, in the Fourier domain, its dynamics should still be dominated by the eigenvector corresponding to the largest eigenvalue $\lambda_2(n^*)$. For this eigenvector, if we take the inverse Fourier transform, we should be able to obtain the long-time dynamics in the spatial domain which can be compared with the results obtained from the I&F model as shown in Fig. 5. Incidentally, we comment that, based on the fact that the function $-\sin(x)/x$ reaches its maximum value around $x = 3\pi/2$ and from Eq. (9), the spatial frequency of the grating pattern can be approximated by $n^* \approx 3/(2p_0)$. This estimation obtained from the simplified system [Eq. (8)] gives $n^* = 15$ for the case of Fig. 5, which is close to its true frequency $n^* = 14$ obtained in the I&F small-world network [Eq. (1)].

Note that we have made two simplifications in our analysis: one is to approximate the small-world structure by the regular-lattice structure, and the other is to approximate the single neuron dynamics with a rectified linear transfer function by its linear dynamics. Because our analysis can well predict the behavior of the original small-world network, it can be concluded that the structure deviation from the small-world network to the regular-lattice network and the nonlinear part of the transfer function have little effect on the fundamental spatial frequency of the original network activity (see more details in Discussion).

Furthermore, to capture the spatial profile of the grating pattern for the case without noise, the analytical solution to Eq. (4) under the large network-size limit can be obtained from an educated guess. As shown in Fig. 6(a), it can be verified that a particular solution in a single period takes the
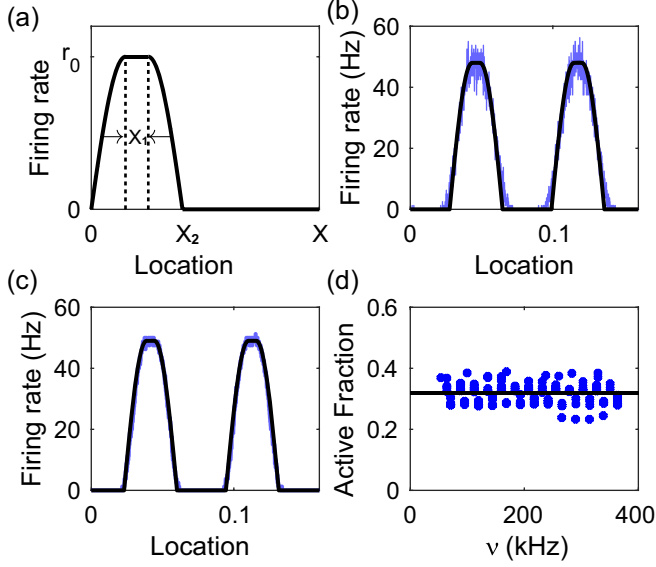
FIG. 6. Analytical solution of the spatial profile of the grating pattern. (a) A particular solution to Eq. (4) for the deterministic case in one spatial period as given in Eq. (10). In (b) and (c), the spatial profiles of the grating pattern (blue line) obtained from the simulations of the I&F small-world neuronal network can be well fitted by the particular solution given in Eq. (10) (black line). Only two spatial periods are presented here. The external input is $f^E = f^I = 0.05$, $\nu^E = \nu^I = 4$ kHz for (b) and $f^E = f^I = 0.001$, $\nu^E = \nu^I = 200$ kHz for (c). Other parameters are the same as in Fig. 2(b). (d) The portion of active neurons in the I&F small-world neuronal network as a function of the external input rate. Blue dots are from the simulations and black line is from the theoretical prediction X_2/X. The corresponding range of population firing rate is from 5 to 50 Hz. In order to reduce the influence of the external input noise, $f^E = f^I = 0.001$. The coupling strength is $J^I = 2J^E = 0.066$.

following form:

$$
r^k(x) = \begin{cases}
r_0 \sin\left(\pi \frac{x}{X_2 - X_1}\right), & 0 \leqslant x < \frac{X_2 - X_1}{2} \\
r_0, & \frac{X_2 - X_1}{2} \leqslant x < \frac{X_2 + X_1}{2} \\
r_0 \cos\left(\pi \frac{x - \frac{X_2 + X_1}{2}}{X_2 - X_1}\right), & \frac{X_2 + X_1}{2} \leqslant x < X_2 \\
0, & X_2 \leqslant x \leqslant X,
\end{cases} \quad (10)
$$

where r_0 is the maximum firing rate, X is the spatial period, X_1 is the width of the platform within which the firing rate of all neurons equals r_0, and X_2 is the width of the active cluster within which the firing rate of all neurons is nonzero. As discussed above, the period of the grating pattern shall be $X = 1/n^*$. By substituting Eq. (10) into Eq. (4), the expression of X_1, X_2, and r_0 in Eq. (10) can be analytically calculated as follows:

$$
X_1 = \left(2X - p_0 - \frac{\pi}{JN}\right)\Big/ 2,
$$

$$
X_2 = \left(2X - p_0 + \frac{\pi}{JN}\right)\Big/ 2,
$$

$$
r_0 = \left(I^{\text{Ext}} - \frac{1}{2}g_L\right)\Big/ (3 + JNX_1). \quad (11)
$$

Here $I^{\text{Ext}} = f\nu$ is the constant external input to each neuron, when we choose $f^E = f^I = f$ and $\nu^E = \nu^I = \nu$ in the simulation. It can be further verified that $r^k(x + \phi)$ with an arbitrary phase value ϕ is the solution to Eq. (7). Figures 6(b) and 6(c) show that Eq. (10) with certain phase can well capture the simulated spatial profile of the neuronal firing rate in the I&F small-world network. And the performance of our analytical solution becomes better when neurons in the network receive less noisy external inputs.

Moreover, as shown in Fig. 6(d), we find that the portion of active neurons in the I&F small-world network is almost unchanged for different levels of external inputs, which is consistent with our theoretical results as shown in Eq. (11). We note that Eq. (10) with any arbitrary phase ϕ is the solution to Eq. (7), indicating that there exists a continuous attractor in the I&F small-world network dynamics. Therefore, noisy input will perturb the network activity along the continuous attractor, which induces the movement of the grating pattern.

C. Diffusivity of the grating pattern

We next investigate the feature of diffusivity of the grating pattern. As shown in a recent experiment [52], the strength of neuronal coupling J scales with the number of connections K as $J \sim \mathcal{O}(1/\sqrt{K})$. Based on this observation, we choose the same scaling as the network size increases, where $K = Np_0$ in our network settings, and derive the dependence of the diffusivity of the grating pattern on the network size. To avoid the unrealistic situations where neurons either generate spikes with very high firing rate or do not spike at all, we make the external input and the cortical input comparable and set the strength of the external input to be $\mathcal{O}(1/\sqrt{K})$ as well, and the external input rate to be $\mathcal{O}(K)$ [53,54]. Under these scalings, the fluctuations of the external input maintain $\mathcal{O}(1)$ as the network size increases.

As discussed above, the network activity has a continuous attractor along the phase variable ϕ. We thus denote the attractor as $\mathbf{r}(\phi)$. If the input is noisy, i.e., with the stochastic Poisson drive, the network activity will be perturbed along the continuous attractor. Therefore, the network response can be characterized as a function of its phase which keeps changing as time evolves, i.e., $\mathbf{r}(\phi(t))$.

On the one hand, the first-order perturbation to the network activity $\mathbf{r}$ with phase ϕ_0 leads to

$$
\mathbf{r}(\phi(t)) = \mathbf{r}(\phi_0) + \frac{d\mathbf{r}(\phi)}{d\phi}\Big|_{\phi=\phi_0} \delta\phi + o(\delta\phi)
$$
$$
= \mathbf{r}(\phi_0) + \mathbf{\Phi}'(\phi_0)\delta\phi + o(\delta\phi), \quad (12)
$$

where $\mathbf{\Phi}$ is a vector with the ith element being the transfer function of the ith neuron, i.e., $\mathbf{\Phi}_i(\phi) = \Phi(\mu_i(\phi))$ and $\mu_i(\phi)$ is the total input to the ith neuron. The derivative $\mathbf{\Phi}'(\phi)$ is with respect to the phase ϕ. The last equality holds because of Eq. (4) in the steady state with a fixed phase value ϕ_0. Therefore, the change of the network activity $\delta\mathbf{r}$ under the perturbation is

$$
\delta\mathbf{r} = \mathbf{\Phi}'(\phi_0)\delta\phi + o(\delta\phi). \quad (13)
$$

On the other hand, under the stochastic input, the change of the network activity $\delta\mathbf{r}$ approximately follows the dynamics

below [substituting Eq. (12) into Eq. (4) with expansion of $\delta \mathbf{r}$]:

$$\tau_r \frac{d\delta \mathbf{r}}{dt} = (\mathbf{K} - \mathbf{I})\delta \mathbf{r} + \sigma \boldsymbol{\eta}, \tag{14}$$

where $K_{ij} = \frac{d\Phi}{d\mu}|_{\mu=\mu_i} J_{ij} C_{ij}$, and $\eta_i = \frac{d\Phi}{d\mu}|_{\mu=\mu_i} \xi_i$ with ξ_i as the standard Gaussian white noise. Note that, in our simulations, the noise originates from the Poisson input. When the input rate is high, the Poisson noise can be well approximated by the Gaussian white noise ξ_i. Correspondingly, the variance of ξ_i takes the value as $\sigma^2 = f^2 \nu$, identical to that of the Poisson noise as we choose $f^E = f^I = f$ and $\nu^E = \nu^I = \nu$ in our simulation.

By substituting Eq. (13) into Eq. (14), we have the following approximate dynamics of $\delta\phi$:

$$\tau_r \boldsymbol{\Phi}'(\phi_0) \frac{d\delta\phi}{dt} = (\mathbf{K} - \mathbf{I})\boldsymbol{\Phi}'(\phi_0)\delta\phi + \sigma \boldsymbol{\eta}. \tag{15}$$

As calculated in the Appendix, $(\mathbf{K} - \mathbf{I})$ has the eigenvalue of zero with a corresponding left eigenvector denoted by $\mathbf{v}$. Note that the dynamics of the system along the continuous attractor mainly correspond to $(\mathbf{K} - \mathbf{I})$ consisting of the zero eigenvalue. We then premultiply both sides of Eq. (15) by the vector $\mathbf{v}$ to obtain

$$\tau_r \mathbf{v}^{\mathbf{T}}\boldsymbol{\Phi}'(\phi_0)\frac{d\delta\phi}{dt} = \mathbf{v}^{\mathbf{T}}(\mathbf{K} - \mathbf{I})\boldsymbol{\Phi}'(\phi_0)\delta\phi + \sigma \mathbf{v}^{\mathbf{T}}\boldsymbol{\eta},$$

and further simplify it by taking the fact of $\mathbf{v}^{\mathbf{T}}(\mathbf{K} - \mathbf{I}) = \mathbf{0}$ to obtain

$$\delta\phi = \frac{\sigma}{\tau_r \mathbf{v}^{\mathbf{T}}\boldsymbol{\Phi}'} \int_0^{\delta T} \mathbf{v}^{\mathbf{T}}\boldsymbol{\eta} \, dt.$$

Because $\mathbf{v}^{\mathbf{T}}\boldsymbol{\eta}$ is Gaussian with zero mean, we can obtain $E(\delta\phi) = 0$, $\text{Var}(\delta\phi) = 2D\delta T$, where the diffusion coefficient D is

$$D = \frac{\sigma^2 \boldsymbol{\Phi}'^{\mathbf{T}}\boldsymbol{\Phi}'}{2\tau_r^2(\mathbf{v}^{\mathbf{T}}\boldsymbol{\Phi}')^2}. \tag{16}$$

As shown in Fig. 7(a), Eq. (16) can well predict the results obtained from the simulations of the I&F small-world neuronal network.

According to the scaling relation between the external input and the network size N, we have $\sigma \sim \mathcal{O}(1)$ independent of network size [48,53–55]. In addition, from the expression of the analytical solution given in Eqs. (10) and (11), for the firing rate of the ith neuron r_i, we have $r_i \sim \mathcal{O}(1)$ and $dr_i/d\phi \sim \mathcal{O}(1)$. The only variable that scales with the network size is the total input μ to each neuron. For the total input to the ith neurons μ_i with $\mu_i > 0$, by taking into account the form of the transfer function, we have $\mu_i = r_i \sim \mathcal{O}(1)$ and $\frac{d\Phi}{d\mu}|_{\mu=\mu_i} = 1$. Therefore, the corresponding elements in $\boldsymbol{\Phi}'$ are expressed as $\Phi_i'(\phi) = \frac{d\Phi_i}{d\mu_i}\frac{d\mu_i}{d\phi} = \frac{dr_i}{d\phi} \sim \mathcal{O}(1)$ and the ith element in $\mathbf{v}^{\mathbf{T}}$ is $v_i \sim \mathcal{O}(1)$ according to Eq. (A2). For the total input to the ith neurons μ_i with $\mu_i < 0$, we have $\frac{d\Phi}{d\mu}|_{\mu=\mu_i} = 0$. In this case, the corresponding elements in $\boldsymbol{\Phi}'^{\mathbf{T}}\boldsymbol{\Phi}'$ and $\mathbf{v}^{\mathbf{T}}\boldsymbol{\Phi}'$ are zero.

Therefore, the inner product of vectors $\boldsymbol{\Phi}'^{\mathbf{T}}\boldsymbol{\Phi}'$, $\mathbf{v}^{\mathbf{T}}\boldsymbol{\Phi}' \sim \mathcal{O}(N)$, and we have that $D \sim \mathcal{O}(\frac{1}{N})$. This scaling relation
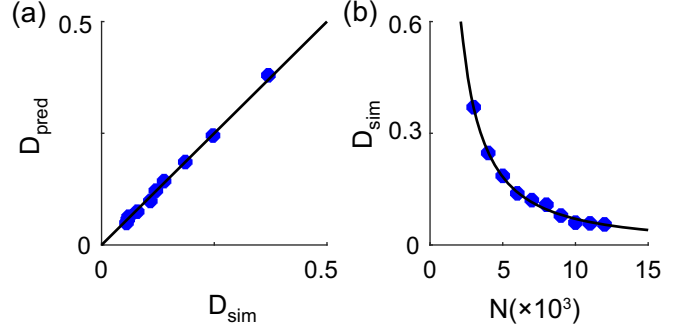

FIG. 7. Diffusion coefficient. (a) Comparison between D_{sim} and D_{pred}. D_{sim} is the diffusion coefficient calculated from the simulation data in the I&F small-world neuronal network and D_{pred} is the diffusion coefficient predicted from Eq. (16). The values of $(D_{\text{pred}}, D_{\text{sim}})$ lie near the black line $y = x$. (b) Diffusion coefficient as a function of network size $2N$. The blue dots are calculated from the simulation of the I&F small-world neuronal network, and the black line is the fit using the inversely proportional function ($\sim\frac{1}{N}$). The parameters are chosen as $J^E = 0.3/\sqrt{Np_0}$, $J^I = 0.6/\sqrt{Np_0}$, $N^E = N^I = N$, $p_0 = 0.1$. The external Poisson input is given to each neuron independently with strength $f^E = f^I = 0.3/\sqrt{Np_0}$ and rate $\nu^E = \nu^I = 30Np_0$.

has been observed in our simulations of the I&F small-world neuronal networks as shown in Fig. 7(b).

V. EXTENSION FOR OTHER NETWORK STRUCTURES

A. Different p_0 for E and I neuronal population

As shown in Fig. 1(b) and Eq. (6), the width of the connectivity profile in our models and simulations is defined as p_0^l for $l = E, I$. Here p_0^l also means that each neuron can have, on average, $N^l p_0^l$ presynaptic neurons in the lth population. It has been found in some experiments that excitatory neurons have broader connectivity profiles than inhibitory neurons [56]. Meanwhile, inhibition has also been found to be more broadly tuned than excitation [57] indicating broader inhibitory projections than excitatory projections. Therefore, it is interesting to investigate how the width of the projections from excitatory and inhibitory neurons affects the network activity.

We next perform simulations of the I&F small-world network by choosing different p_0^E and p_0^I for E and I populations, respectively. As shown in Fig. 8, the spatial frequency of the grating pattern is almost independent of p_0^E but is dependent on p_0^I. This fact can be intuitively understood from the expression of λ_2:

$$\lambda_2(n) = -1 + J^E N^E p_0^E \frac{\sin\left(\pi n p_0^E\right)}{\pi n p_0^E} - J^I N^I p_0^I \frac{\sin\left(\pi n p_0^I\right)}{\pi n p_0^I}.$$

If the inhibition is much stronger than the excitation, i.e., $J^E N^E p_0^E \ll J^I N^I p_0^I$, the second term is negligible compared with the third term in the above expression. Therefore, the spatial frequency of the grating pattern n^* at which $\lambda_2(n)$ reaches its maximum value is mainly determined by the third term involving p_0^I only. In our simulations, we find that $n^* \approx \frac{3}{2p_0^I}$ is almost independent of p_0^E even when the inhibition is
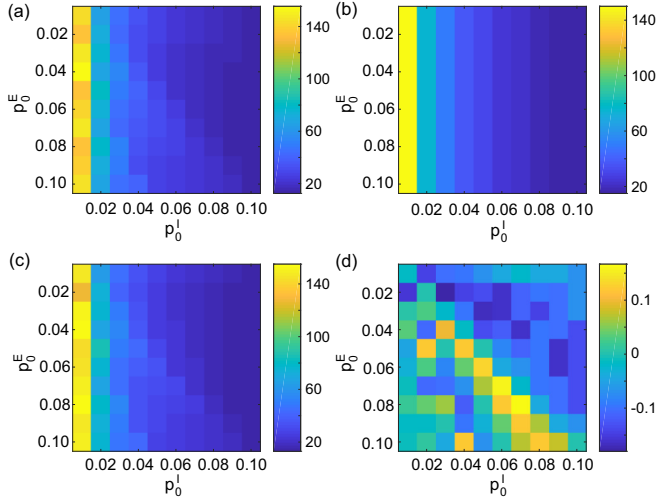
FIG. 8. Spatial frequency n^* as a function of parameters p_0^E and p_0^I. The spatial frequency n^* is analytically calculated as the value at which $\lambda_2(n)$ reaches its maximum in (a), approximated as $3/(2p_0^I)$ in (b), and directly computed from simulation data of the I&F small-world neuronal network in (c). The relative errors between the simulation results and the approximated value $3/(2p_0^I)$ are shown in (d). The parameters are chosen as $J^I N^I p_0^I = 2J^E N^E p_0^E$ and the network size is $N^E = N^I = 4000$.

only twice larger in magnitude than the excitation as shown in Figs. 8(b)–8(d).

B. Small-world networks in higher dimensions

To investigate whether our results can be generalized to small-world networks in higher dimension, we next consider the small-world network in the two-dimensional state space $(0, 1] \times (0, 1]$. In the two-dimensional space, the distance between the neuron at location (x_i, y_i) and the neuron at location (x_j, y_j) can be calculated as $d_{ij} = \sqrt{2(d_x^2 + d_y^2)}$ with $d_x = \min(|x_i - x_j|, 1 - |x_i - x_j|)$ in the x direction, and $d_y = \min(|y_i - y_j|, 1 - |y_i - y_j|)$ in the y direction. The network connection is then generated with the probability identical to Eq. (3).

We simulate a two-dimensional small-world network with I&F neurons. As shown in Fig. 9(a), the network activity is qualitatively similar to that of the one-dimensional network. If the cortical input strength is large, neurons form active clusters whose movement resembles diffusive waves. We further generalize our results to the three-dimensional space and observe similar phenomena in the three-dimensional I&F small-world network as shown in Fig. 9(b). The analysis in Sec. IV can also be generalized to the two-dimensional and three-dimensional cases. To be specific, the connectivity kernel has the form of the circular disk in the two-dimensional space and the form of the ball in the three-dimensional space. Then, for the two-dimensional case, in the Fourier domain, one can obtain

$$\lambda_2^{2d}(\rho) = -1 + \frac{J^E N^E}{\rho} r_c^E \mathbb{J}_1\big(2\pi \rho r_c^E\big) - \frac{J^I N^I}{\rho} r_c^I \mathbb{J}_1\big(2\pi \rho r_c^I\big),$$
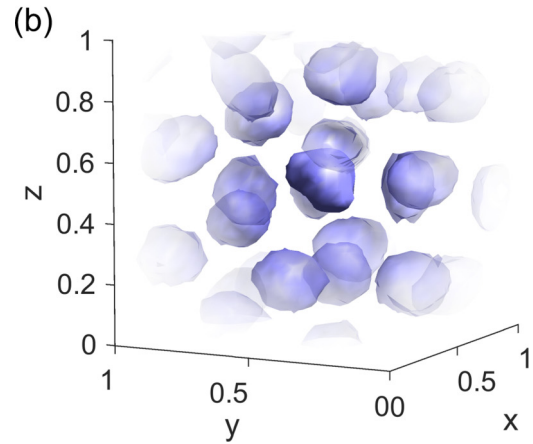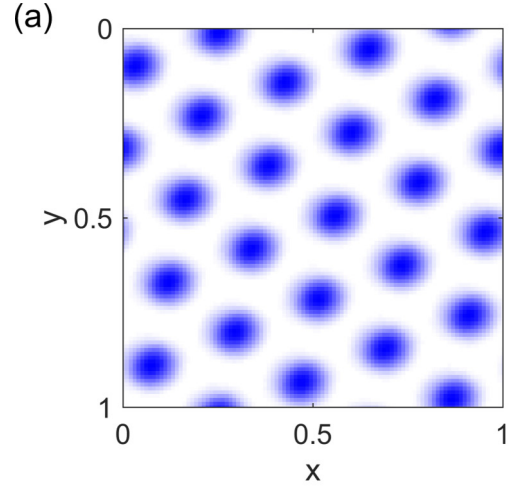

FIG. 9. Simulations of I&F small-world neuronal networks in higher dimensions. (a) is for a two-dimensional network of size $N^E = N^I = 10^4$ and $J^I = 2J^E = 0.04$, $f^E = f^I = 0.02$, $\nu^E = \nu^I = 10$ kHz. (b) is for a three-dimensional network of size $N^E = N^I = 2.7 \times 10^4$, $J^I = 2J^E = 0.07$, $f^E = f^I = 0.03$, $\nu^E = \nu^I = 8$ kHz. Color codes active neurons in a short period of 400 ms in (a) and neurons with firing rate larger than 10 Hz (for ease of illustration) in 400 ms in (b). Other parameters are $p_0^E = p_0^I = 0.08$.

where $\rho = \sqrt{n_x^2 + n_y^2}$ with frequency variables n_x and n_y according to the x and y directions, $r_c^I = \sqrt{N^I p_0^I / \pi}$ for $l = E, I$, and $\mathbb{J}_1(\cdot)$ is the first-order Bessel function of the first kind. Similarly, for the three-dimensional case, one can obtain

$$\lambda_2^{3D}(\rho) = \frac{J^E N^E}{2\pi^2 \rho^3} \sin\big(2\pi \rho r_c^E\big) - \frac{J^E N^E r_c^E}{\pi \rho^2} \cos\big(2\pi \rho r_c^E\big)$$
$$- \frac{J^I N^I}{2\pi^2 \rho^3} \sin\big(2\pi \rho r_c^I\big) + \frac{J^I N^I r_c^I}{\pi \rho^2} \cos\big(2\pi \rho r_c^I\big) - 1,$$

where $\rho = \sqrt{n_x^2 + n_y^2 + n_z^2}$ with three frequency variables n_x, n_y, and n_z according to three directions, and $r_c^I = \sqrt[3]{(3N^I p_0^I)/(4\pi)}$ for $l = E, I$. Our results find that the value of ρ^* corresponding to the largest eigenvalue obtained from

the above formulas can well predict the spatial frequency of the grating pattern in the numerical simulations of the I&F small-world neuronal network.

VI. DISCUSSION

By simulating the dynamics of strongly coupled I&F neuronal networks with the small-world structure, we have observed that the network activity generates spatially periodic diffusive waves. We have then performed a theoretical analysis to understand the emergence, the spatial frequency, and the diffusion coefficient of the waves observed in I&F small-world networks by using the approximated firing-rate-based neuronal networks.

Based on the eigenvalue analysis, we find that the difference between the small-world network and the regular-lattice network is small. Intuitively, the small difference between the two networks results from the fact that the small-world network is generated by rewiring very few connections in the regular-lattice network. Based on this, our analysis can be carried out and a continuous attractor has been identified to explain the dynamical phenomena observed in the simulations. It shall be pointed out that small-world networks can be generated in various ways [58–60]. It is possible that the small-world network generated in other ways may deviate from the network generated through the effective rewiring of the regular-lattice network in our work. In such a case, differences in network dynamics are expected between these small-world networks and the regular-lattice network.

Note that we approximate the dynamics of I&F neuronal networks by a firing-rate-based neuronal network with the rectified linear transfer function. However, certain experimental observations suggest that the transfer function follows a rectified power-law function [61]. The power usually lies between 2 and 5 [62]. From our simulations of the firing-rate-based neuronal network, we find that the power of the transfer function will change the amplitude of the grating pattern but not its frequency. It will also not affect the critical coupling strength above which the grating pattern emerges. However, we should point out that, from our simulations, it has been observed that our analysis may fail when the majority of neurons in the network do not receive enough external input to fire. In such a case, the total inputs to most neurons can be negative, which falls into the nonlinear part of the transfer function.

It has already been known that a ring network can generate spatially periodic patterns, and the emergence of the spatial patterns is associated with a zero eigenvalue [19,48]. However, our work is not merely a reproduction of these phenomena. In addition to these, we have derived the explicit expressions of the spatial frequency of the pattern in both an exact form and an approximated form, the firing rate profile as a function of neuron location under the condition of strong coupling [Eqs. (10) and (11)], and have discovered the phenomenon of diffusive waves and calculated the diffusive coefficient of the network dynamics when all the neurons receive independent Poisson noisy inputs [Eq. (16)].

Our work suggests that a small-world neuronal network can behave similarly to a regular-lattice neuronal network. However, this result does not necessarily indicate that small world is similar to regular lattice in any sense both dynamically and functionally. In fact, we have demonstrated that the similarity between small-world and regular-lattice network dynamics mainly exists in the particular dynamical regime and condition where neurons receive strong inhibition from their presynaptic neurons and independent external noisy inputs. Under this condition, the dynamics of the small-world neuronal network is dominantly affected by the high clustering property of the small-world network. This result indeed complements previous works investigating the dynamics in a small-world neuronal network in different dynamical regimes and conditions. For instance, if the inhibitory coupling strength weakens, the self-sustained dynamics emerges [31]. If the external inputs become coherent, distant neuronal groups start to synchronize globally [30]. Under those conditions, the dynamics of the small-world network is also substantially affected by the short path length property of the small-world network [32,63–65], thus being different from the dynamics of the regular-lattice network.

In addition, we note that many previous works have investigated the regular-lattice network models with exponential, Gaussian, or Mexican-hat connectivity kernels to understand brain dynamics such as waves, bumps, and patterns [20,66–68]. In these models, the dynamical phenomena rely on either broader inhibition than excitation [66,67] or global inhibition [20,68] to form particular patterns. Here we consider a square kernel in our work, and show that the spatial pattern occurs when the coupling is sufficiently strong, insensitive to the width of the connectivity kernel. Therefore, our result provides a simple alternative mechanism to generate waves in a network. Nevertheless, it should be pointed out that the waves observed in the real brain may have much more complicated structures rather than being spatially periodic. Therefore, the quantitative comparison between simulated neuronal network dynamics and the cerebral cortical dynamics remains to be further investigated in the future.

ACKNOWLEDGMENTS

APPENDIX

Here we show that the matrix $(\mathbf{K} - \mathbf{I})$ in Eq. (14) has the eigenvalue zero, and we calculate the corresponding left eigenvector denoted by $\mathbf{v}$.

Note that, at the steady state of the firing-rate-based system Eq. (4), we have

$$\frac{d\mu_i}{d\phi}\bigg|_{\phi=\phi_0} = \sum_j J_{ij}C_{ij}\frac{dr_j}{d\phi}\bigg|_{\phi=\phi_0},$$

$$\frac{dr_i}{d\phi}\bigg|_{\phi=\phi_0} = \frac{d\Phi}{d\mu_i}\frac{d\mu_i}{d\phi}\bigg|_{\phi=\phi_0}.$$

Thus

$$\sum_j J_{ij}C_{ij}\frac{d\Phi}{d\mu_j}\frac{d\mu_j}{d\phi}\bigg|_{\phi=\phi_0} - \frac{d\mu_i}{d\phi}\bigg|_{\phi=\phi_0} = 0. \qquad (A1)$$

In a regular-lattice network, we have the following relation (which approximately holds in a small-world network):

$$J_{ij}C_{ij} = \begin{cases} J_{ji}C_{ji} & i \leqslant N^E, j \leqslant N^E \\ -\frac{J^E}{J^I}J_{ji}C_{ji} & i \leqslant N^E, j > N^E \\ -\frac{J^I}{J^E}J_{ji}C_{ji} & i > N^E, j \leqslant N^E \\ J_{ji}C_{ji} & i > N^E, j > N^E \end{cases}$$

Thus, for $i \leqslant N^E$, Eq. (A1) has the form as

$$\sum_{j\leqslant N^E} J_{ji}C_{ji}\frac{d\Phi}{d\mu_j}\frac{d\mu_j}{d\phi}\bigg|_{\phi=\phi_0} - \frac{J^E}{J^I}\sum_{j>N^E} J_{ji}C_{ji}\frac{d\Phi}{d\mu_j}\frac{d\mu_j}{d\phi}\bigg|_{\phi=\phi_0}$$

$$- \frac{d\mu_i}{d\phi}\bigg|_{\phi=\phi_0} = 0,$$

for $i > N^E$,

$$\sum_{j\leqslant N^E} J_{ji}C_{ji}\frac{d\Phi}{d\mu_j}\frac{d\mu_j}{d\phi}\bigg|_{\phi=\phi_0} - \frac{J^E}{J^I}\sum_{j>N^E} J_{ji}C_{ji}\frac{d\Phi}{d\mu_j}\frac{d\mu_j}{d\phi}\bigg|_{\phi=\phi_0}$$

$$+ \frac{J^E}{J^I}\frac{d\mu_i}{d\phi}\bigg|_{\phi=\phi_0} = 0.$$

Therefore, $\mathbf{v^T}(\mathbf{K} - \mathbf{I}) = \mathbf{0}$ holds, where $\mathbf{v}$ has the ith element as

$$v_i = \begin{cases} \frac{d\mu_i(\phi)}{d\phi}\big|_{\phi=\phi_0}, & i \leqslant N^E \\ -\frac{J^E}{J^I}\frac{d\mu_i(\phi)}{d\phi}\big|_{\phi=\phi_0}, & i > N^E. \end{cases} \qquad (A2)$$

That is, $\mathbf{v^T}$ is the left eigenvector of the matrix $(\mathbf{K} - \mathbf{I})$ for the eigenvalue zero.

---

[1] J.-Y. Wu, X. Huang, and C. Zhang, Neuroscientist **14**, 487 (2008).

[2] L. Muller and A. Destexhe, J. Physiol. (Paris) **106**, 222 (2012).

[3] L. Muller, F. Chavane, J. Reynolds, and T. J. Sejnowski, Nat. Rev. Neurosci. **19**, 255 (2018).

[4] J. Zheng, S. Lee, and Z. J. Zhou, Nat. Neurosci. **9**, 363 (2006).

[5] L. Muller, A. Reynaud, F. Chavane, and A. Destexhe, Nat. Commun. **5**, 3675 (2014).

[6] Y. Penn, M. Segal, and E. Moses, Proc. Natl. Acad. Sci. USA **113**, 3341 (2016).

[7] S. Li, J. Xu, G. Chen, L. Lin, D. Zhou, and D. Cai, Sci. Rep. **7**, 5637 (2017).

[8] A. R. Backus, J.-M. Schoffelen, S. Szebényi, S. Hanslmayr, and C. F. Doeller, Curr. Biol. **26**, 450 (2016).

[9] M. Steriade, I. Timofeev, and F. Grenier, J. Neurophysiol. **85**, 1969 (2001).

[10] A. Luczak, P. Barthó, S. L. Marguet, G. Buzsáki, and K. D. Harris, Proc. Natl. Acad. Sci. USA **104**, 347 (2007).

[11] X. Chen, N. L. Rochefort, B. Sakmann, and A. Konnerth, Cell Rep. **4**, 31 (2013).

[12] A. Arieli, A. Sterkin, A. Grinvald, and A. Aertsen, Science **273**, 1868 (1996).

[13] M. A. Kisley and G. L. Gerstein, J. Neurosci. **19**, 10451 (1999).

[14] T. Kenet, D. Bibitchkov, M. Tsodyks, A. Grinvald, and A. Arieli, Nature (London) **425**, 954 (2003).

[15] N. Brunel, Network: Comput. Neural Syst. **11**, 261 (2000).

[16] S. Kang, K. Kitano, and T. Fukai, Neural Networks **17**, 307 (2004).

[17] N. Brunel, J. Comput. Neurosci. **8**, 183 (2000).

[18] R. Ali, J. Harris, and B. Ermentrout, Phys. Rev. E **94**, 012412 (2016).

[19] J. D. Harris and B. Ermentrout, Phys. D **369**, 30 (2018).

[20] A. Compte, N. Brunel, P. S. Goldman-Rakic, and X.-J. Wang, Cereb. Cortex **10**, 910 (2000).

[21] Y. Burak and I. R. Fiete, PLoS Comput. Biol. **5**, e1000291 (2009).

[22] O. Sporns and J. D. Zwi, Neuroinformatics **2**, 145 (2004).

[23] E. Bullmore and O. Sporns, Nat. Rev. Neurosci. **10**, 186 (2009).

[24] M. E. Newman, SIAM Rev. **45**, 167 (2003).

[25] D. J. Watts and S. H. Strogatz, Nature (London) **393**, 440 (1998).

[26] D. J. Felleman and D. E. Van, Cereb. Cortex **1**, 1 (1991).

[27] J. Scannell, G. Burns, C. Hilgetag, M. O'Neil, and M. P. Young, Cereb. Cortex **9**, 277 (1999).

[28] P. Hagmann, M. Kurant, X. Gigandet, P. Thiran, V. J. Wedeen, R. Meuli, and J.-P. Thiran, PloS One **2**, e597 (2007).

[29] D. S. Bassett and E. Bullmore, Neuroscientist **12**, 512 (2006).

[30] N. Masuda and K. Aihara, Biol. Cybern. **90**, 302 (2004).

[31] A. Roxin, H. Riecke, and S. A. Solla, Phys. Rev. Lett. **92**, 198101 (2004).

[32] T. I. Netoff, R. Clewley, S. Arno, T. Keck, and J. A. White, J. Neurosci. **24**, 8075 (2004).

[33] V. J. Barranca, H. Huang, and G. Kawakita, J. Comput. Neurosci. **46**, 145 (2019).

[34] M. Kuperman and G. Abramson, Phys. Rev. Lett. **86**, 2909 (2001).

[35] D. H. Zanette, Phys. Rev. E **65**, 041908 (2002).

[36] C. Moore and M. E. J. Newman, Phys. Rev. E **61**, 5678 (2000).

[37] D. Cai, A. V. Rangan, and D. W. McLaughlin, Proc. Natl. Acad. Sci. USA **102**, 5868 (2005).

[38] A. V. Rangan, D. Cai, and D. W. McLaughlin, Proc. Natl. Acad. Sci. USA **102**, 18793 (2005).

[39] K. A. Newhall, G. Kovačič, P. R. Kramer, D. Zhou, A. V. Rangan, and D. Cai, Commun. Math. Sci. **8**, 541 (2010).

[40] D. Zhou, A. V. Rangan, D. W. McLaughlin, and D. Cai, Proc. Natl. Acad. Sci. USA **110**, 9517 (2013).

[41] D. Zhou, A. V. Rangan, Y. Sun, and D. Cai, Phys. Rev. E **80**, 031918 (2009).

[42] D. Zhou, Y. Sun, A. V. Rangan, and D. Cai, J. Comput. Neurosci. **28**, 229 (2010).

[43] H. F. Song and X.-J. Wang, Phys. Rev. E **90**, 062801 (2014).

[44] R. Brette, M. Rudolph, T. Carnevale, M. Hines, D. Beeman, J. M. Bower, M. Diesmann, A. Morrison, P. H. Goodman, F. C. Harris *et al.*, J. Comput. Neurosci. **23**, 349 (2007).

[45] A. Destexhe, J. Comput. Neurosci. **27**, 493 (2009).

[46] B. Kriener, H. Enger, T. Tetzlaff, H. E. Plesser, M.-O. Gewaltig, and G. T. Einevoll, Frontiers Comput, Neurosci. **8**, 136 (2014).

[47] A. Renart, J. De La Rocha, P. Bartho, L. Hollender, N. Parga, A. Reyes, and K. D. Harris, Science **327**, 587 (2010).

[48] R. Rosenbaum and B. Doiron, Phys. Rev. X **4**, 021039 (2014).

[49] A. Roxin, N. Brunel, and D. Hansel, Phys. Rev. Lett. **94**, 238103 (2005).

[50] E. Ledoux and N. Brunel, Frontiers Comput. Neurosci. **5**, 25 (2011).

[51] D. Jercog, A. Roxin, P. Bartho, A. Luczak, A. Compte, and J. de la Rocha, Elife **6**, e22425 (2017).

[52] J. Barral and A. D. Reyes, Nat. Neurosci. **19**, 1690 (2016).

[53] C. v. Vreeswijk and H. Sompolinsky, Neural Comput. **10**, 1321 (1998).

[54] Q. L. Gu, Z. K. Tian, G. Kovacic, D. Zhou, and D. Cai, Frontiers Comput. Neurosci. **12**, 47 (2018).

[55] C. Van Vreeswijk and H. Sompolinsky, Science **274**, 1724 (1996).

[56] R. B. Levy and A. D. Reyes, J. Neurosci. **32**, 5609 (2012).

[57] G. K. Wu, R. Arbuckle, B.-h. Liu, H. W. Tao, and L. I. Zhang, Neuron **58**, 132 (2008).

[58] P. Gong and C. van Leeuwen, Europhys. Lett. **67**, 328 (2004).

[59] M. Kaiser and C. C. Hilgetag, Phys. Rev. E **69**, 036103 (2004).

[60] N. Jarman, C. Trengove, E. Steur, I. Tyukin, and C. van Leeuwen, Cogn. Neurodyn. **8**, 479 (2014).

[61] N. J. Priebe, F. Mechler, M. Carandini, and D. Ferster, Nat. Neurosci. **7**, 1113 (2004).

[62] N. J. Priebe and D. Ferster, Neuron **57**, 482 (2008).

[63] S. N. Ching, E. N. Brown, and M. A. Kramer, Phys. Rev. E **86**, 021920 (2012).

[64] L. F. Lago-Fernández, R. Huerta, F. Corbacho, and J. A. Sigüenza, Phys. Rev. Lett. **84**, 2758 (2000).

[65] H. Riecke, A. Roxin, S. Madruga, and S. A. Solla, Chaos **17**, 026110 (2007).

[66] S. Coombes, Biol. Cybern. **93**, 91 (2005).

[67] P. C. Bressloff, J. Phys. A: Math. Theor. **45**, 033001 (2012).

[68] M. Tsodyks, Hippocampus **9**, 481 (1999).